

Studying dark gaps in Ly- α forest transmission with large reionization simulation

Barun Maity^{1,*}, Frederick B. Davies¹, Benedetta Spina² and Sarah E. I. Bosman²

¹ Max-Planck-Institut für Astronomie, Königstuhl 17, D-69117 Heidelberg, Germany

² Institute for Theoretical Physics, Heidelberg University, Philosophenweg 12, D-69120, Heidelberg, Germany

Received XXX; accepted XXX

ABSTRACT

The physical conditions of the intergalactic medium (IGM) during the final stages of cosmic reionization ($z \sim 5.0 - 6.0$) are not yet fully understood. Recent reports of unexpectedly large-scale ($\geq 150 h^{-1} \text{cMpc}$) correlation in Ly- α transmission flux using extended XQR-30 quasar spectra pose interesting consequences on the reionization end stages. In this work, we investigate the Ly- α forest dark-gap distribution (defined as regions with transmitted flux below 0.05) as another sensitive tracer of the IGM, using an efficient, large-volume ($\sim 1 \text{ Gpc}$) simulation framework. By constructing a suite of physically motivated model variants (i.e., varying the reionization redshift, IGM temperature, and ionizing-photon mean free path), we generate synthetic sightlines and compare their predicted cumulative distribution of dark gaps with that of observed spectra (at redshift intervals of $\Delta z = 0.2$). We find that most of the models achieve qualitatively consistent agreement with the data. Specifically, the scenario involving a slightly later reionization completion ($z \sim 5.4$) provides the closest match, while a short constant mean free path model disfavors the data at lower redshifts. These findings give further support for the emerging scenario of reionization end extending to $z \leq 5.7$, although they can not rule out a slightly early reionization with enhanced post-ionization ultraviolet (UV) background fluctuations. A similar conclusion arises from the redshift distribution of long dark gap ($L \geq 30 h^{-1} \text{cMpc}$) fraction. However, the model variants are still not able to reproduce the observed strong flux correlations at unusually large scales, which remains open for further investigations.

Key words. intergalactic medium – cosmology: theory – dark ages, reionization, first stars – large-scale structure of Universe

1. Introduction

The Epoch of Reionization (EoR) forms a critical bridge between the early and present-day Universe, preserving the imprints of the first luminous sources. During this epoch, the collective radiation from those sources drove the transformation of the intergalactic medium (IGM) from an almost entirely neutral state following recombination to a highly ionized one. Although substantial theoretical and observational advances have been made, the detailed morphology, duration, and physical processes governing the EoR remain among the most significant open questions in contemporary cosmology (see reviews for details, Barkana & Loeb 2001; Choudhury 2009; McQuinn 2016; Dayal & Ferrara 2018; Gnedin & Madau 2022; Choudhury 2022).

A diverse set of observational probes has been developed to constrain the neutral fraction of the IGM during the reionization era. These include measurements based on the damping wing signatures observed in quasars (e.g., Davies et al. 2018; Greig et al. 2019, 2022, 2024; Wang et al. 2020) and galaxies (e.g., Umeda et al. 2024, 2025a) spectra, Lyman (Ly)- α emitters luminosity functions (e.g., Morales et al. 2021; Kageura et al. 2025) and their clustering properties (e.g., Sobacchi & Mesinger 2015; Umeda et al. 2025b), as well as Ly- α equivalent widths (e.g., Mason et al. 2018; Jones et al. 2025), collectively probing redshifts up to $z \lesssim 12.0$. These studies generally point to a midpoint of reionization $z_{\text{re}} \sim 7.0 - 8.0$ (Hoag et al. 2019; Bañados et al. 2018), although the derived constraints are often limited by uncertainties in continuum modeling of the underlying

spectra. Complementarily, at relatively lower redshifts ($z \lesssim 6.0$), more robust constraints have emerged from dark-pixel fraction analyses (Jin et al. 2023; Davies et al. 2025) and from damping-wing signatures identified in stacked Ly- α forest spectra (Spina et al. 2024; Zhu et al. 2024). Moreover, the pronounced large-scale fluctuations observed in the Ly- α forest effective opacity distribution (τ_{eff}) suggest that the reionization may extend towards lower redshifts, even below $z < 5.5$ (Kulkarni et al. 2019; Bosman et al. 2022).

A range of theoretical models has been proposed to account for the excess fluctuations observed in the Ly- α forest opacity at lower redshifts. Under the assumption that the IGM is already highly ionized in this regime, these fluctuations may arise from residual inhomogeneities in the temperature field (D'Aloisio et al. 2015) and/or from spatial variations in the ultraviolet background (UVB) driven by a relatively short ionizing-photon mean free path (Davies & Furlanetto 2016; Maity et al. 2025). Alternatively, the most widely discussed explanation invokes the presence of residual neutral islands, implying that reionization concluded later than traditionally assumed (Keating et al. 2020; Nasir & D'Aloisio 2020; Choudhury et al. 2021; Qin et al. 2025). This scenario is also supported by the rapid evolution of photon mean free path at $6.0 \geq z \geq 5.0$ (Becker et al. 2021), as well as large-scale underdensities associated with long dark troughs (e.g., $\sim 110 h^{-1} \text{cMpc}$ of ULAS J0148+0600; Becker et al. 2015) traced by the spectra of Ly- α emitters (Christenson et al. 2023) and Ly-break galaxies (Kashino et al. 2020). Nevertheless, these observations do not rule out an early-reionization scenario characterized by substantial UVB fluctuations (Zhu et al. 2021).

* maity@mpia.de

Therefore, key questions concerning the influence and spatial extent of neutral islands at these lower redshifts remain unresolved. Improved measurements of Ly- α forest opacity fluctuations and their redshift evolution may offer a promising avenue for breaking the degeneracy among competing models. Additional complementary constraints can be obtained from the statistics of dark gaps (defined as contiguous regions where the transmitted flux falls below a specified threshold) in the forest, which may arise either from persistent neutral patches or from regions permeated by a relatively weak UV background (e.g., Fan et al. 2006; Gallerani et al. 2008; Gnedin et al. 2017; Nasir & D'Aloisio 2020). Recent efforts involving dark gaps statistics in Ly- α forest also indicate strong degeneracy between these models (Zhu et al. 2021). However, earlier studies were limited by the modest sizes of the simulation volumes employed ($\leq 160 h^{-1}$ cMpc), constrained by computational cost and model complexity (e.g., Gnedin et al. 2017; Zhu et al. 2021). More recently, an unexpectedly large-scale correlation in the Ly- α forest ($\geq 150 h^{-1}$ cMpc) has been reported (Spina et al. 2025) using the extended (E)-XQR-30 dataset (D'Odorico et al. 2023). This finding motivates the use of substantially larger simulation volumes, such as the BIBORTON box ($\sim 1024 h^{-1}$ cMpc), capable of capturing fluctuations on the relevant scales, in combination with the efficient Ly- α forest modeling framework developed by Maity et al. (2025). Nevertheless, the fiducial large-box model fails to reproduce the observed large-scale correlations within the range of currently understood physical mechanisms (Spina et al. 2025).

To address these issues, we extend our investigation by exploring a suite of model variants within large-volume simulations. In particular, we examine scenarios that differ in the timing of reionization completion, the amplitude of UVB fluctuations, and the thermal state of the IGM. Our goal is to evaluate the performance of these models against the other known observables derived from Ly- α forest, such as statistics using dark pixel distributions at the redshift range $5.0 \leq z \leq 6.1$. We utilized 42 high S/N quasar spectra from the E-XQR-30 dataset, after carefully avoiding the contamination due to damped Ly- α (DLA) and O-VI lines, and compared them with our model predictions. This study thus provides an important robustness test of the different model realizations, thereby reinforcing the interpretations suggested by current observational findings.

The paper is organized as follows. In Section 2, we briefly discuss the simulation methodology, introducing different variants of the model parameters. We lay out the data reduction procedure to get the dark pixel distribution in Section 3. Following this, we discuss the statistics that have been studied in Section 4. We summarize our findings and interpretations subsequently in the Section 5. Finally, we conclude the work in Section 6. Throughout this paper, we use h^{-1} cMpc as distance unit unless otherwise stated and adopt Planck Collaboration et al. (2020) values of cosmological parameters ($\Omega_m = 0.308$, $h = 0.678$, $\Omega_\Lambda = 0.691$).

2. Simulation in brief

2.1. Methodology

The simulation methodology utilized in this study has been exploited and described in a recent study by Spina et al. (2025). The discussion in this section closely follows the simulation description of that earlier work. To better understand the physical mechanisms at play during the late EoR, we aim to compare our observational results with physically motivated simu-

lations of the intergalactic medium IGM. Ideally, this would require a simulation volume with both high dynamic range, preserving large-scale correlations, while also resolving small-scale physics. However, achieving this level of detail is computationally prohibitive with current resources.

As an alternative, we adopt a complementary strategy, applying a semi-numerical technique developed by Maity et al. (2025). This method efficiently produces large-volume lightcones of Ly α transmission across the redshift range $z = 4.9$ – 6.2 (spanning a comoving length of approximately $420 h^{-1}$ cMpc), which is well-suited to our study.

In our semi-numerical framework, the Ly- α optical depth is modeled as a function of underlying cosmological density fluctuations, UVB variations, temperature inhomogeneities, and ionization fluctuations (where reionization remains incomplete). These relationships are calibrated against a high-resolution, fully hydrodynamic simulation—specifically, the Nyx code (Almgren et al. 2013). The semi-numerical UVB and reionization models additionally require the collapsed halo mass fraction (f_{coll}) to estimate the available ionizing photon budget. For this purpose, we generate density fields at fixed redshift using the Zel'dovich approximation (Zel'dovich 1970) in a large computational volume ($L = 1024 h^{-1}$ Mpc). The collapsed mass fraction field is calculated in Lagrangian space via the Excursion Set Formalism (ESF-L; Trac et al. 2022). This combination reproduces large-scale structure consistent with full N-body simulations while allowing efficient exploration of EoR evolution.

The ionization and temperature histories are then evolved using the photon-conserving reionization model SCRIPT, which includes recombination effects (Maity & Choudhury 2022a). In this model, the temperature increment due to photoionization heating is associated with a free parameter, T_{re} , and the available photon budget is determined by the ionizing efficiency, ζ (assuming a power-law variation with redshift). For computational practicality, we do not explicitly model radiative feedback; instead, its influence is approximated by enforcing a fixed minimum halo mass ($M_{\text{min}} = 10^9 M_\odot$), below which structure formation is suppressed.

Our simulations employ a spatial resolution of $\Delta x = 4 h^{-1}$ Mpc, balancing computational efficiency and accuracy. To track lightcone evolution, we produce simulation snapshots at intervals of $\Delta z = 0.1$, interpolating between them as needed. Given the density and source fields, we apply the EX-CITE model (Gaikwad et al. 2023) to generate UVB fluctuations, incorporating local source contributions as described in Davies & Furlanetto (2016); Davies et al. (2024). This process is controlled by two key parameters: the effective mean free path of ionizing photons (λ_{mfp}) and the average photoionization rate ($\langle \Gamma_{\text{HI}} \rangle$). All these quantities are utilized to get the transmission flux lightcones via the calibrated Fluctuating Gunn Peterson Approximation (FGPA) as detailed in Maity et al. (2025). We tune the mean photoionization rate for each coeval boxes such that the mean transmission flux match the estimates of Bosman et al. (2022).

2.2. Model suite

In this section, we describe the suite of models employed to compute the dark-pixel statistics. The models are outlined below:

– **fiducial:** This model corresponds to a realistic scenario where reionization ends at $z \sim 5.6$ – 5.7 and the IGM temperatures are modelled in a self-consistent way as described in Maity et al. (2025). This corresponds to a temperature increment parameter (T_{re}) of $10^{4.2} K$. The mean free path param-

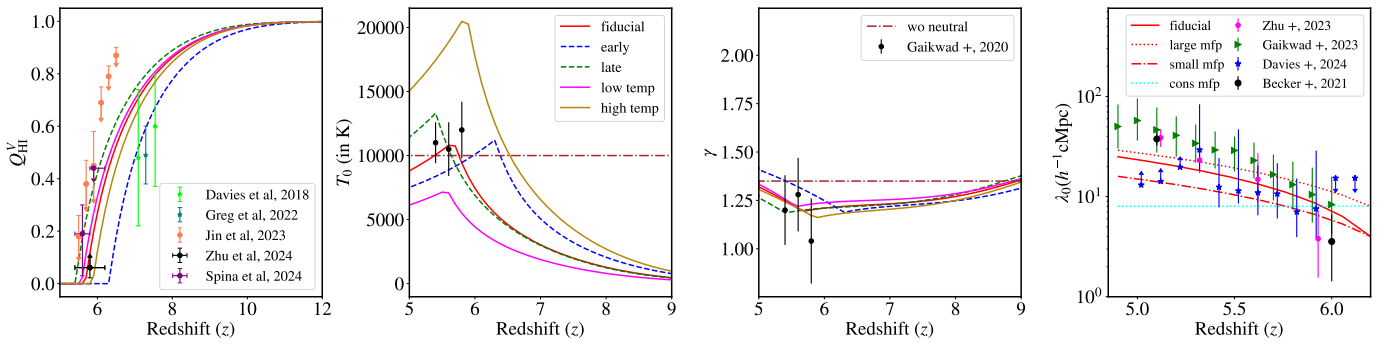


Fig. 1. Different observables for the various model scenarios assumed in this study. From left to right, the panels show redshift evolution of global neutral fraction (Q_{HI}^V), mean IGM temperature (T_0), index of temperature-density relation (γ) and the effective photon mean free path (λ_0). We also show various constraints on these quantities, as suggested by recent studies, i.e, constraints on neutral fraction (Davies et al. 2018; Greig et al. 2022; Jin et al. 2023; Spina et al. 2024; Zhu et al. 2024), IGM temperature estimates (Gaikwad et al. 2020), mean free path estimates (Becker et al. 2021; Gaikwad et al. 2023; Zhu et al. 2023; Davies et al. 2024).

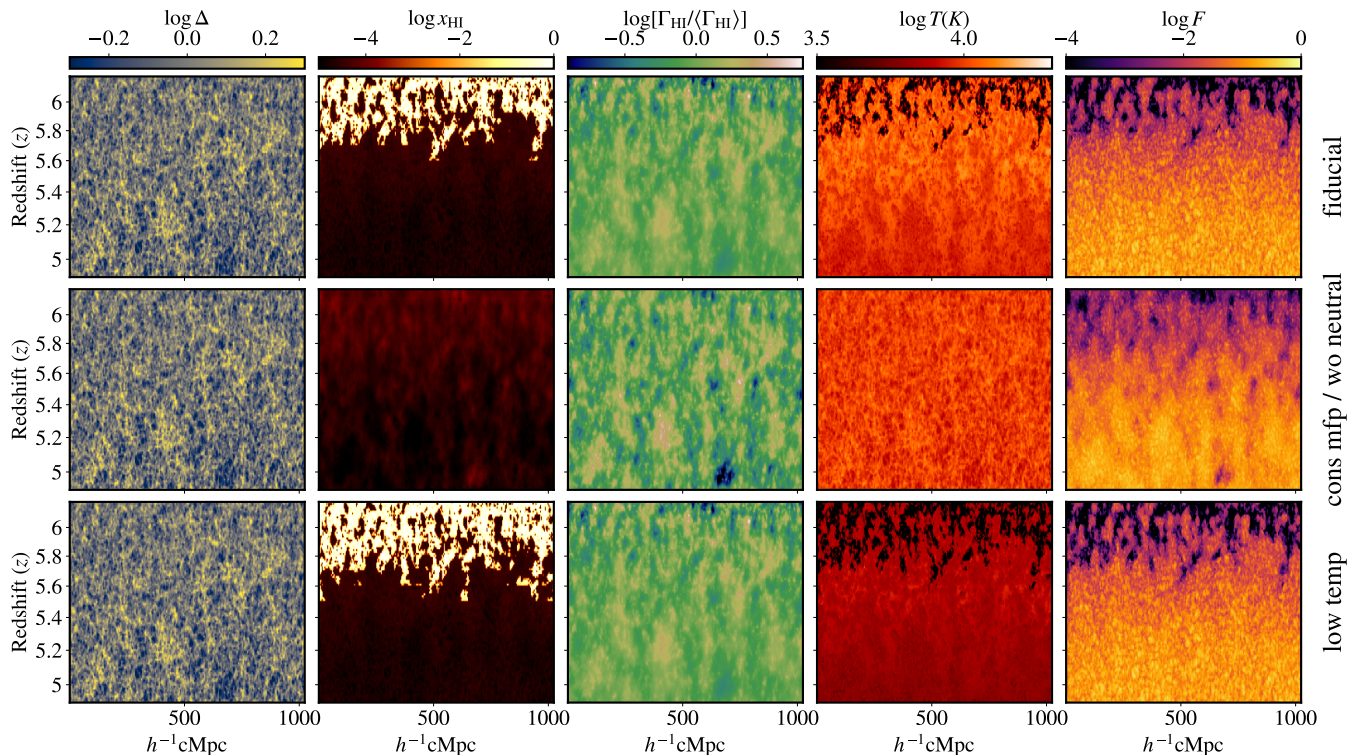


Fig. 2. Lightcone snapshots for three different cases in (top: fiducial, middle: cons mfp / wo neutral, and bottom: low temp) in three rows. The columns correspond to density (Δ), neutral fractions (x_{HI}), UVB fluctuations ($\Gamma_{\text{HI}}/\langle\Gamma_{\text{HI}}\rangle$), temperature (T), and flux (F). The colorbars have been shown in logarithmic scales. The rest of the scenarios has been shown in Appendix A.

eter (λ_0) evolves from $4 h^{-1}\text{cMpc}$ at $z = 6.2$ to $25 h^{-1}\text{cMpc}$ at $z = 4.9$. The fiducial model obeys the recent observational constraints on ionization and temperature evolution.

- **early:** This is a variant of the fiducial model in which reionization ends earlier, at $z \sim 6.3$. The earlier completion is achieved by increasing the ionizing-efficiency parameter, ζ , while retaining the self-consistent thermal and ionization evolution.
- **late:** This corresponds to a complementary variant where reionization ends slightly late (at $z \sim 5.4$). This is realized by reducing the ionizing-efficiency parameter relative to the fiducial case.
- **large mfp:** This model is designed to explore reduced UVB inhomogeneity, achieved by increasing the mean free path at

every redshift by $4 h^{-1}\text{cMpc}$ relative to the fiducial values (same reionization end as fiducial).

– **small mfp** This scenario adopts a reduced mean free path than the fiducial, thereby increasing UVB fluctuations. Specifically, λ_0 evolves from $15 h^{-1}\text{cMpc}$ at $z = 5.0$ to $4 h^{-1}\text{cMpc}$ at $z = 6.2$. This scenario is also closer to the estimates of Maity et al. (2025), based on Ly- α forest opacity fluctuations at the intermediate redshifts ($z \sim 5.4 - 5.7$).

– **cons mfp / wo neutral:** In this model, no residual neutral islands are assumed to exist in the targeted redshift interval, and correspondingly, no temperature evolution are introduced. The IGM temperature follows a standard equation of state, $T = T_0 \Delta^{\gamma-1}$, with $T_0 = 10^4 \text{ K}$ and $\gamma = 1.35$. We also

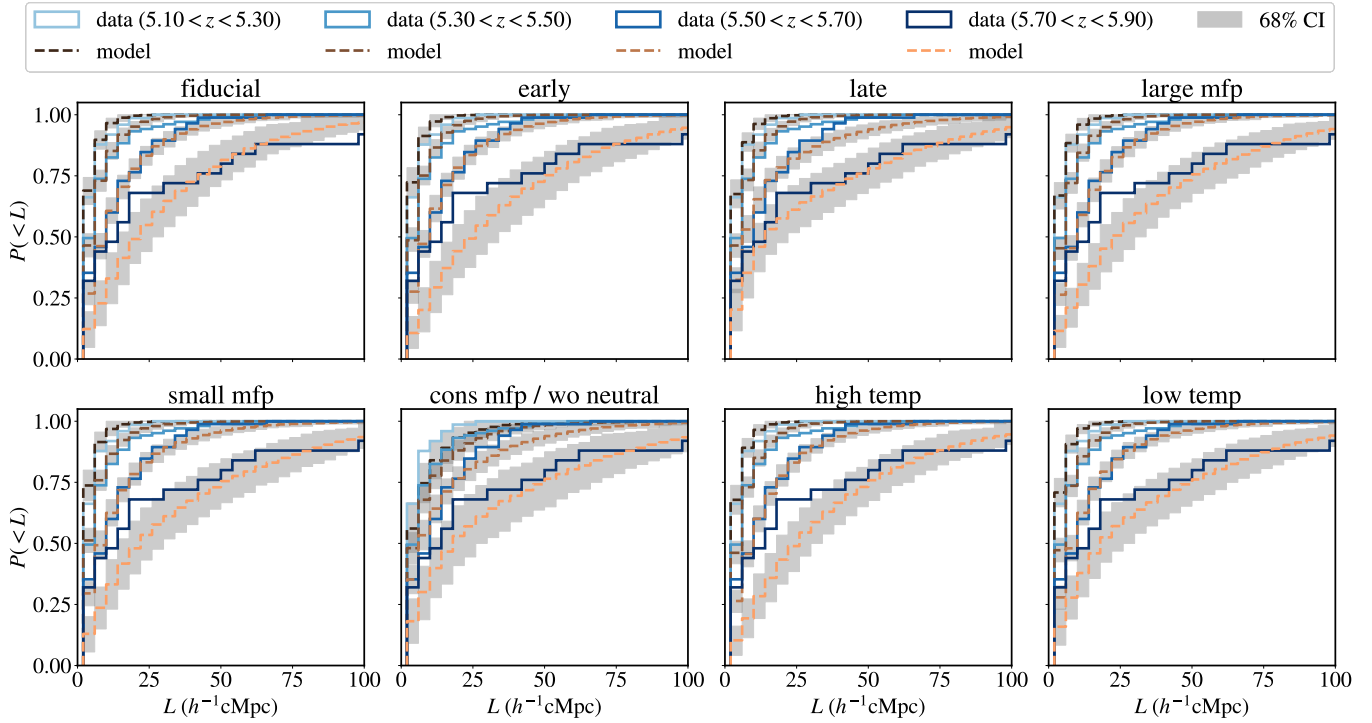


Fig. 3. The cumulative probability distribution functions (CDFs) of dark gap lengths at different redshift ranges (within an interval of $\Delta z = 0.2$), corresponding to the set of different model variants, discussed in section 2.2. The *solid* lines denote the derived distribution from the observed data, while the *dashed* lines are the corresponding predictions using model skewers. The shaded region signifies 68% uncertainties on the model distributions.

use a constant λ_0 of $8 h^{-1}\text{cMpc}$ throughout the redshift range instead of evolution.

- **high temp:** This corresponds to a high-heating scenario in which the T_{re} parameter is set to $3 \times 10^4 \text{ K}$, which is substantially higher than the fiducial case. This corresponds to a slightly earlier reionization end than the fiducial due to the reduced strength of recombination.
- **low temp:** This is a complementary version of the previous case, with cooler IGM (fixing T_{re} at 10^4 K), which is considerably smaller than the fiducial scenario. This pushes the reionization end towards slightly lower redshift than the fiducial scenario due to stronger recombination.

In Figure 1, we present the ionization histories, temperature evolution, and mean free path evolution for all model variants described above. As expected, the fiducial model satisfies the available observational constraints, while the alternative variants diverge in ways consistent with their construction. For instance, the early reionization model doesn't obey the nearly model-independent constraints on neutral fraction (Jin et al. 2023; Spina et al. 2024). The models with lower (higher) temperature produce an IGM temperature (T_0) well below (above) the estimates of Gaikwad et al. (2020). These deviations highlight the parameter sensitivity of the thermal and ionization histories and their probable influence on the predicted Ly- α forest observables.

In Figure 2, we further illustrate the spatial distribution of the key physical quantities through snapshots (i.e., neutral fraction, UVB fluctuations, temperature, and transmission flux) corresponding to three representative model variants (i.e., fiducial, cons mfp /wo neutral, and low temp, from top to bottom row). Notably, lowering the temperature has only a minimal impact on the transmitted-flux morphology (i.e., top and bottom rows), without strongly affecting large-scale opacity. By contrast, the

absence of mean free path evolution or neutral island (i.e., middle row) can produce a substantially different flux field. Specifically, the flux field is much smoother without the effect of neutral island and can produce dark regions that persist even at a redshift of $z \sim 5.0$ due to existing strong UVB fluctuations (as a consequence of relatively short mean free path).

These comparisons emphasize that certain physical ingredients, such as the presence of residual neutral islands and the redshift evolution of the mean free path, play a dominant role in shaping large-scale Ly- α forest opacity fluctuations. Consequently, dark-pixel statistics may provide a sensitive diagnostic for distinguishing among these scenarios.

3. Observational data

We use a sample of the observational dataset described in Spina et al. (2025) implementing the reduction procedures, consisting of the 42 high-redshift quasar spectra at $z > 5.5$ with $\text{S/N} \geq 10$ per $\leq 15 \text{ km s}^{-1}$ pixel of the E-XQR-30 sample (Bosman et al. 2022; D’Odorico et al. 2023). The spectra were obtained with VLT/X-Shooter (Vernet et al. 2011) and reduced following the procedures outlined in Bosman et al. (2022). Each sightline is continuum-normalized using the near-linear log-PCA method of Davies et al. (2018) and Bosman et al. (2021, 2022), which reproduces the intrinsic continuum with $\sim 8\%$ accuracy and well-characterized wavelength-dependent uncertainties. All spectra are rebinned into $4 h^{-1}\text{Mpc}$ intervals to keep it consistent with the simulations, and non-detections are retained to preserve the noise statistics.

We apply the same masking strategy as in Spina et al. (2025), excluding rest-frame wavelengths $\lambda > 1185 \text{ \AA}$ to avoid proximity-zone contamination, masking all damped Ly- α sys-

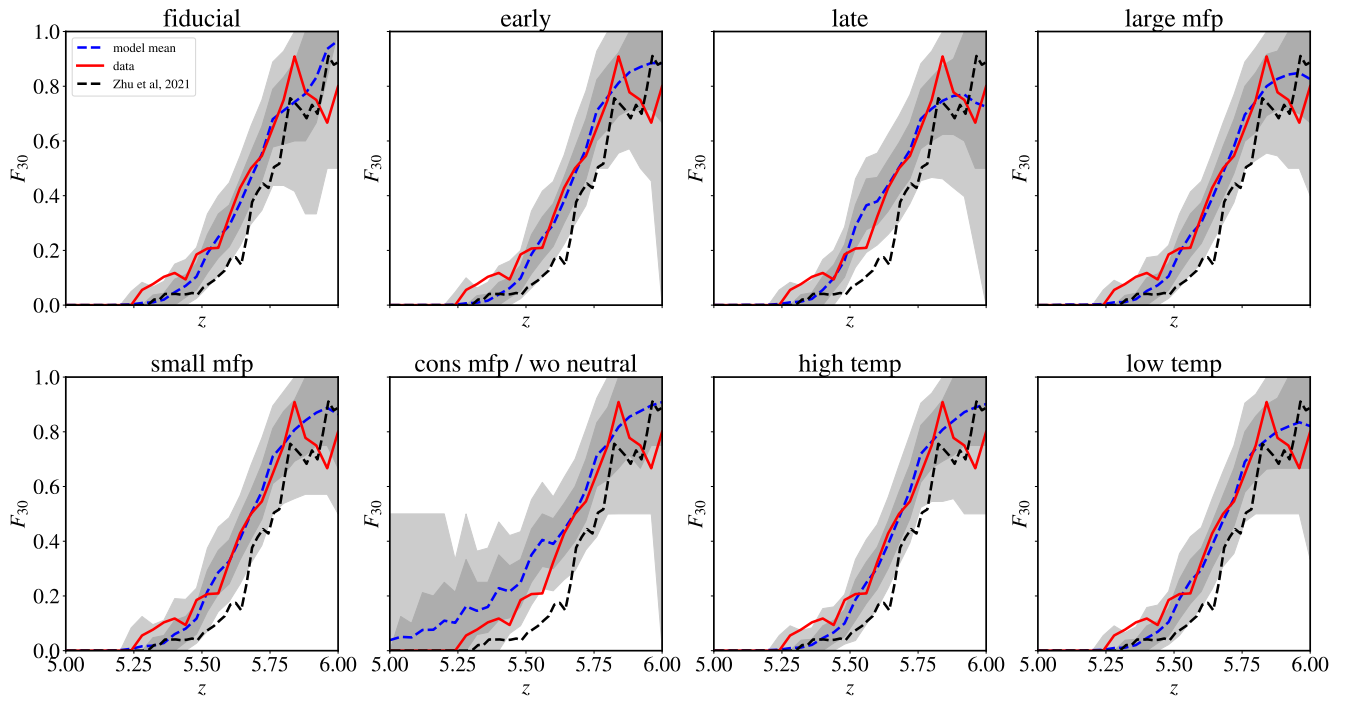


Fig. 4. Fraction of skewers with dark gap length, $L \geq 30 h^{-1}\text{cMpc}$ (F_{30}) as a function of redshift (z) for the different model variants, discussed in section 2.2. The red lines are derived distributions from the observed spectra. The blue dashed lines denote the mean distribution after averaging over skewer realizations from the model suites. The shaded regions show the corresponding 68% and 95% uncertainties. In black dashed, we show similar estimates from an earlier study (Zhu et al. 2021), with different skewer resolution and samples.

tems (DLAs) identified in Davies et al. (2023), and removing all pixels within $\Delta v = 5000 \text{ km s}^{-1}$ of the redshifted $\text{O VI} \lambda\lambda 1032, 1038 \text{ \AA}$ emission line to prevent spurious large-scale correlations. Residual sky-line contamination and all other cleaning steps described in Bosman et al. (2022) are applied identically.

As discussed in Spina et al. (2025), we verified that the large-scale correlations observed in the data are not produced by continuum-reconstruction uncertainties. This was tested using 1000 mock realizations of the QSO sample, in which the continuum of each sightline is perturbed by coherent Gaussian offsets matched to the measured continuum uncertainties. These mocks reproduce the mild correlation seen at $z \lesssim 5.3$ but fail to generate the strong, extended correlations detected at higher redshift, even when the continuum-uncertainty amplitude is artificially increased by 50%. This demonstrates that the correlations observed in the data reflect genuine large-scale structure in the IGM rather than systematics arising from continuum fitting.

4. Statistics with flux skewers

We employ three complementary statistics in this work, each designed to capture large-scale information encoded in the Ly- α forest. The first two are the cumulative distribution function (CDF) of dark-gap lengths in different redshift intervals and the fraction of spectra (or skewers) containing long dark gaps as a function of redshift. These statistics are motivated by earlier observational analyses, e.g., Zhu et al. (2021). The third is the correlation-coefficient matrix of the Ly- α transmitted flux across redshift bins, recently introduced by (Spina et al. 2025), which was also the main motivation for utilizing these large box simulations. We extract N ($=15000$) random flux skewers from the lightcone volumes, covering a redshift range, $z = 4.9\text{--}6.2$. These

are divided into multiple realizations of 42 sets (to mimic the observed dataset), which are further used to compute the statistics. Specifically, we use 1000 realizations to compute the bootstrap uncertainties on the dark gap statistics. Furthermore, we remove all the dark skewers from the analysis (both data and models) that hit the boundary of the lightcone redshift ranges, to keep the estimators robust. Below, we briefly introduce each of the statistics by summarizing the computation procedures.

4.1. CDF of dark gap lengths

This statistic characterizes the average distribution of dark gaps within a given redshift interval. We define a pixel as dark if its transmitted flux falls below the threshold ($F \leq 0.05$ in this study). Consecutive dark pixels are grouped to form a dark gap, whose physical length is obtained by summing the number of pixels within the gap and weighing by the pixel resolution. Once we have the distribution of dark gaps, we assign them a central redshift value that corresponds to the middle of their extent. We then divide the distribution into four redshift bins with an interval of $\Delta z = 0.2$, from $z = 5.1$ to $z = 5.9$. The uncertainties on these distributions are computed by bootstrapping the skewer realizations. We compare the CDFs of the dark gap lengths in these intervals utilizing our simulated spectra and the spectra from the E-XQR-30 dataset. While computing the dark gaps from observational data, we follow the same procedure as we did for the simulation, which makes the comparison consistent with each other. Specifically, the observational spectra are averaged over $4 h^{-1}\text{cMpc}$ scale to match the resolution of our simulation. In the observed dataset, the non-detected pixels are assumed to be a part of dark gaps if they fall between two consecutive dark

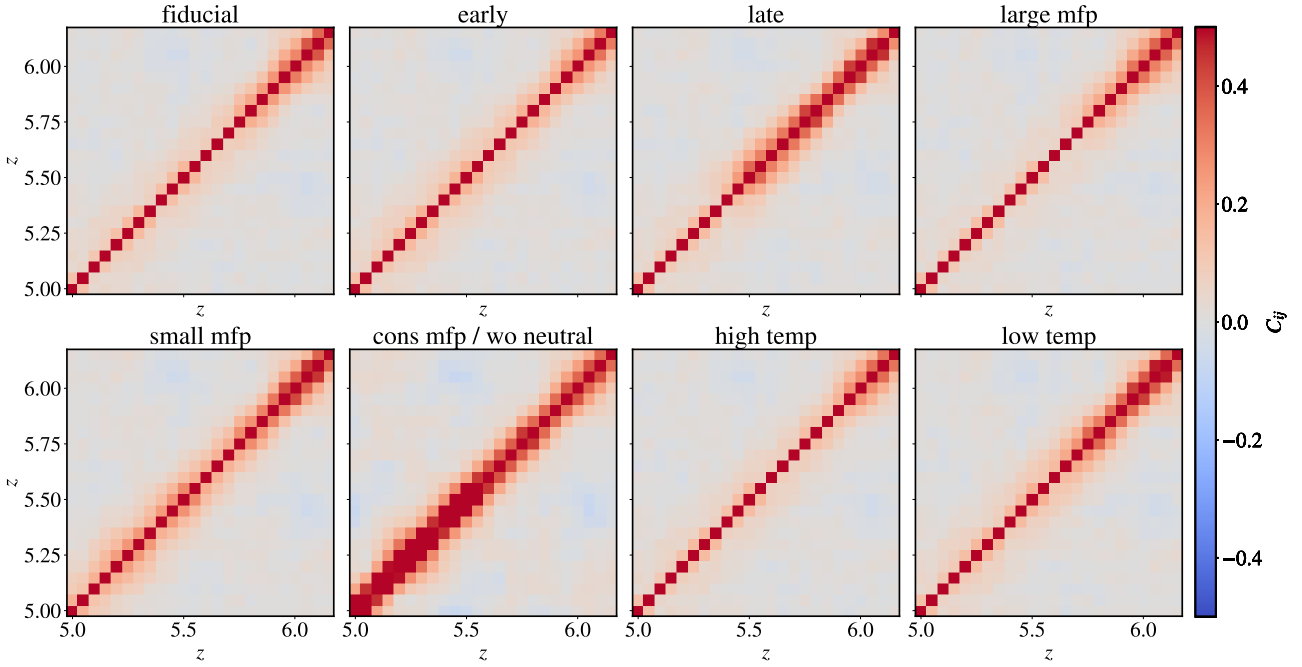


Fig. 5. Correlation coefficients of the transmission flux between redshift ranges considered in this study ($z = 5.0 - 6.1$). The panels show the different scenarios, as discussed in section 2.2. The correlation matrix derived from 67 quasar sightlines (including E-XQR-30 samples) has been reported in Spina et al. (2025).

patches. Otherwise, we mask those pixels from the analysis procedures.

4.2. Evolution of dark gap fraction

The redshift evolution of long dark gaps serves as a sensitive diagnostic of residual neutral patches and UVB-fluctuation strength at late times. To estimate the fraction of skewers exhibiting long dark gaps, we check for the presence of dark pixels which are part of a long gap ($L \geq 30h^{-1}\text{cMpc}$) in each redshift interval (Δz) of 0.02 and count the numbers. Then we divide the count of skewers providing long gaps by the total number of skewers in the corresponding range to estimate the fraction, F_{30} . We compute this fraction as a function of redshift, which provides a quantification of the dark gap frequencies with redshift evolution. Notably, we remove the possible contamination of damped Ly- α systems and metal absorbers from the dataset (as discussed in Section 3) to make the comparison with simulations as consistent as possible.

4.3. Correlation Matrix

This estimator reveals the large-scale correlation in the observed transmitted flux, which sets the motivation of the work. Similar to Spina et al. (2025), we bin the skewers with a redshift interval of $\Delta z = 0.05$. If $F_{i,j}$ is the flux value for i -th binned skewer at redshift bin j , the covariance matrix is estimated as

$$S_{ij} = \sum_{k=1}^N (F_{k,i} - \langle F \rangle_i)^T (F_{k,j} - \langle F \rangle_j) \quad (1)$$

where $\langle \dots \rangle$ represents the average over all the skewers (i.e. $N = 15000$ in our case). This further provides the correlation matrix

as

$$C_{ij} = \frac{S_{ij}}{\sqrt{S_{ii}S_{jj}}} \quad (2)$$

Specifically, we look for the behavior of off-diagonal terms, where a strong positive enhancement would suggest correlated structures among redshift bins.

5. Results & interpretations

In this section, we present our results and provide a qualitative discussion of how the different model variants impact the three statistics introduced earlier.

In Figure 3, we show the CDFs of the dark gap lengths across different redshift intervals. The solid curves represent the distributions derived from the observed E-XQR-30 sightlines, while the dashed ones correspond to mean predictions from our model skewers. The shaded region shows the 68% uncertainty in the distribution by sampling different model realizations. Overall, the fiducial model reproduces the observed trends well across all redshift bins. Specifically, at the highest redshift interval, $5.7 \leq z \leq 5.9$, the model correctly mimics the distribution width towards large dark gap lengths ($L \geq 25h^{-1}\text{cMpc}$), while it slightly underpredicts the abundance of shorter gaps. The relative lack of short length gaps at the corresponding redshift range points towards the lack of small neutral islands in the fiducial model. This is also evident from the "late" end model, where the relative number of short length gaps is larger, yielding an improved match with the data. Not surprisingly, the deviation is slightly more pronounced for the "early" scenario due to a lower neutral fraction. Similarly, the model with a lower temperature slightly improves the distribution by elevating the number of small dark gaps at higher redshifts. Not surprisingly, the higher

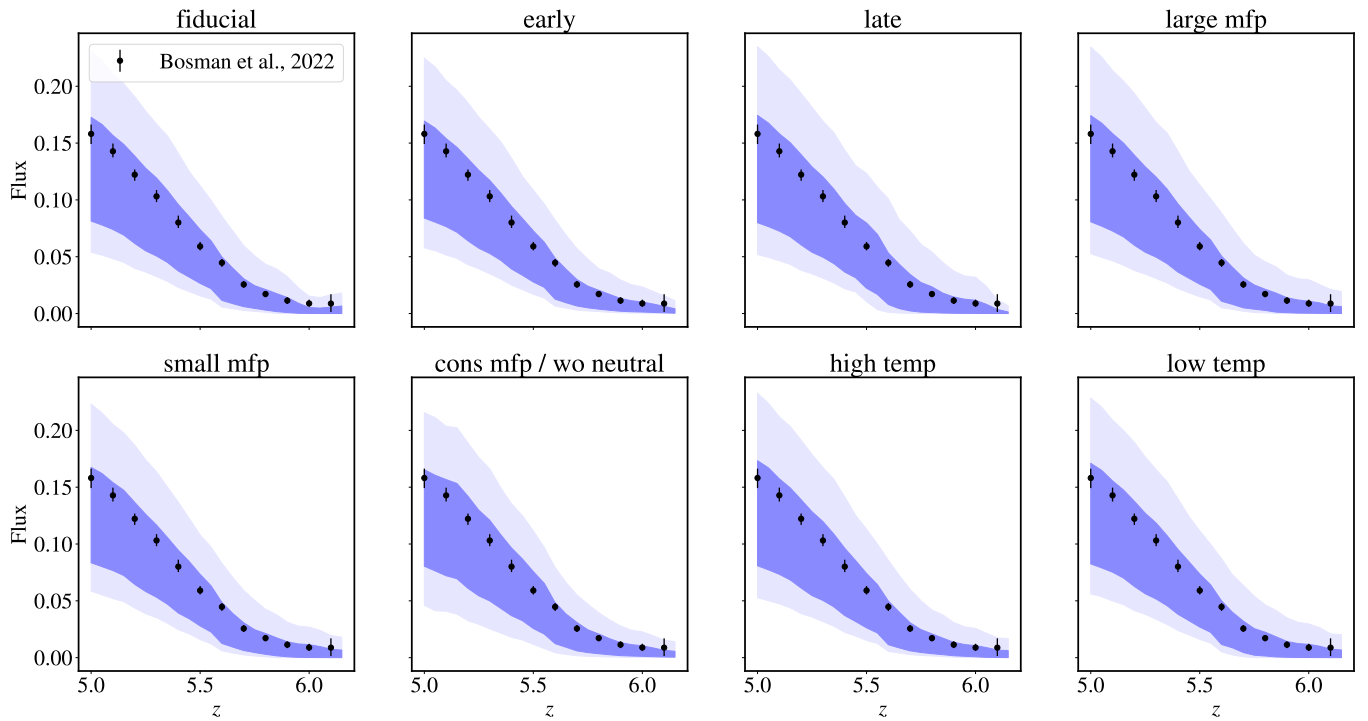


Fig. 6. Flux distribution as a function of redshift, for the different scenarios as discussed in section 2.2. The bands show the 68% and 95% intervals of the flux distributions in the extracted skewers. The mean fluxes of the coeval simulation boxes have been matched with the observed mean, shown in black points (Bosman et al. 2022).

temperature model degrades the match as it provides a slightly earlier reionization end and fewer dark gaps. The models with a larger or a smaller mean free path do not affect these statistics much, providing similar trends as the fiducial one. However, a redshift evolving λ_0 is necessary to match the shape of the distribution at lower redshift intervals (i.e., $5.1 \leq z \leq 5.7$). This can be reconciled from the "cons mfp / wo neutral" case, where the model predicts too many dark gaps at lower redshifts, disfavoring the data distribution at the interval $5.1 \leq z \leq 5.3$.

Next, in Figure 4, we show the data and model comparison using F_{30} statistics as defined earlier. The red lines correspond to the data distribution, while the dashed blue lines are the estimates from the models. The estimates of Zhu et al. (2021) differ slightly (black dashed) from this work due to differences in the assumed pixel resolution of the flux skewers and the number of sources. For all the cases, the dark fraction value increases as we move towards higher redshifts, signifying the increased presence of large opaque regions. The data reveal the emergence of long dark gaps beginning at $z = 5.3$, which is consistent with the recent findings of large-scale opacity fluctuations at those redshifts. We also find that the model variants of different reionization ends (i.e., "fiducial", "early", and "late") do not affect the distribution significantly and provide consistent trends with the derived estimates from observed quasar spectra. Likewise, models incorporating temperature changes or modifications to the photon mean free path do not produce significant deviations from the fiducial behavior, offering limited constraining power in these parameter spaces. We note that the data indicate a slight tension with respect to the mean predictions of the models at the redshifts $z \approx 5.3 - 5.5$, by producing an elevated long dark gap fraction. This excess may hint at the persistence of sizable neutral patches at these redshifts, although the current sample size limits the statistical significance of this feature. In

agreement with the discussion in the previous paragraph, "cons mfp/wo neutral" predicts a larger fraction of long dark gaps even at lower redshift ($z < 5.3$) with a large uncertainty. This comes as a consequence of the assumed small (and constant) mean free path throughout the redshifts. However, as discussed earlier, this scenario is already disfavored by the CDF distributions at lower redshifts. Overall, these estimators can not fully alleviate the degeneracy between the different models, providing a consistent picture with earlier studies (Zhu et al. 2021).

We present the correlation matrix between the redshift bins in Figure 5. This exploration is motivated by the observed large-scale correlation¹ reported by Spina et al. (2025). Their measurements indicate that the characteristic correlation scale increases toward higher redshifts, reaching values as large as $\gtrsim 150 h^{-1}\text{cMpc}$. This corresponds to a redshift bin interval $\Delta z_{\text{bin}} \gtrsim 0.3$ at a typical redshift of $z = 5.7$. However, neither of our model variants is able to produce such a large correlation length. Although the fiducial scenario does exhibit a modest redshift evolution of the correlation, its amplitudes and scales fall well short of the observed estimates (Spina et al. 2025). The correlation length scale increases a bit in the presence of the neutral islands for the late ending case, but that again is not sufficient to explain the observed correlation. Similarly, the usage of a short mean free path model slightly inflates the correlations across redshifts, but fails to match the data. These discrepancies suggest that a more comprehensive exploration of the model parameter space is required, possibly involving more sophisticated physical treatments. Fully numerical hydrodynamical simulations are the ideal avenue for such an investigation, although the box size requirement ($\gtrsim 500 h^{-1}\text{cMpc}$) remains computa-

¹https://drive.google.com/file/d/1cR4YBad9td00xKaPp3vSfqh1cLPJhLUY/view?usp=share_link

tionally prohibitive. However, we can still play with other inherent assumptions within the semi-numerical setup. For instance, our models assume a fixed fiducial power law dependence of the mean free path on density ($\propto \Delta^{-1}$) and photoionization rate ($\Gamma_{\text{HI}}^{2/3}$), while generating the UVB fluctuations. We need to check how the variations on these relationships affect the large-scale correlations. The other implications include cosmological modifications of the underlying density field, which may demand an involvement of non-standard physics at those redshifts. From the observational side, it is necessary to increase the number of quasar spectra for more robust estimates of the statistics and check the persistence of large-scale correlations utilizing larger samples.

Finally, in Figure 6, we show the flux distribution of the skewers as a function of redshift. It is apparent that all the models obey the observed mean transmission fluxes, which have been imposed by the construction of these model variants. The widths of the distributions are very similar, which makes it not suitable for distinguishing between models.

6. Summary and conclusions

The final stages of the epoch of reionization remain an open question in modern cosmology. Recent observational evidence, particularly the detection of large-scale fluctuations in Ly- α forest opacity, appears to favor a relatively late end to reionization. However, sufficient room exists for a relatively early end, but the fluctuations are driven by post-ionization UVB background. Motivated by the large-scale Ly- α transmission correlations reported by Spina et al. (2025), we employ a gigaparsec-scale simulation framework for modeling Ly- α forest opacity distributions, based on the efficient semi-numerical method of Maity et al. (2025). Using this setup, we investigate the statistical properties of dark pixels in the Ly- α forest flux by comparing the observed high-redshift quasar spectra from the E-XQR-30 sample and the variants of our large simulation boxes. Our main conclusions are summarized below:

- We constructed eight model variants (including the fiducial one) by varying different model ingredients such as mean free path, reionization end, and temperatures. The fiducial model was chosen such that it obeys a variety of recent observational constraints during the late phase of the EoR. In each case, the models were tuned to match the mean transmission fluxes at the redshift ranges ($5.0 \leq z \leq 6.1$) covered in this study.
- We utilized these models to compare the CDF of the dark gap (defined as contiguous pixels with flux below 0.05) distributions with the samples from E-XQR-30 dataset. We found that our fiducial model provides a reasonable match to the data, while the variant with slightly late reionization end and lower temperature improves the agreement. On the contrary, the data seem to disfavor the model with a short and constant mean free path without any presence of neutral island towards lower redshift bins ($z < 5.5$).
- We further compared the fraction of skewers with long dark gaps ($\geq 30 h^{-1}\text{cMpc}$) as a function of redshift. The model variants again provide excellent matches to the data. We found a slight tension in the redshift range $5.3 - 5.5$, where the data indicate a relatively large fraction of long dark gaps. However, this remains statistically inconclusive, and we need more samples for any further conclusions.
- Lastly, following our original motivation, we checked the correlation coefficients between the redshift bins. We found

that none of our model variants produce an extremely large-scale correlation as reported by Spina et al. (2025). This suggests that the observed correlation may have cosmological implications beyond the standard realm. However, a more detailed exploration of the model parameters by alleviating astrophysical assumptions is necessary for any further conclusions.

The study provides a robustness check of our large-scale Ly- α forest simulation model against the cutting-edge observations of dark gap distribution during late phase of reionization. In the future, the models will be useful to strategise large-scale survey of high-redshift IGM.

Data Availability

The data presented in this article will be shared on reasonable request to the corresponding author (BM).

References

Almgren, A. S., Bell, J. B., Lijewski, M. J., Lukić, Z., & Van Andel, E. 2013, ApJ, 765, 39

Bañados, E., Venemans, B. P., Mazzucchelli, C., et al. 2018, Nature, 553, 473

Barkana, R. & Loeb, A. 2001, Phys. Rep., 349, 125

Becker, G. D., Bolton, J. S., Madau, P., et al. 2015, MNRAS, 447, 3402

Becker, G. D., D’Aloisio, A., Christenson, H. M., et al. 2021, MNRAS, 508, 1853

Bosman, S. E. I., Davies, F. B., Becker, G. D., et al. 2022, MNRAS, 514, 55

Bosman, S. E. I., Davies, F. B., Becker, G. D., et al. 2021, arXiv e-prints, arXiv:2108.03699

Choudhury, T. R. 2009, Current Science, 97, 841

Choudhury, T. R. 2022, General Relativity and Gravitation, 54, 102

Choudhury, T. R., Paranjape, A., & Bosman, S. E. I. 2021, MNRAS, 501, 5782

Christenson, H. M., Becker, G. D., D’Aloisio, A., et al. 2023, ApJ, 955, 138

D’Aloisio, A., McQuinn, M., & Trac, H. 2015, ApJ, 813, L38

Davies, F. B., Bosman, S. E. I., D’Odorico, V., et al. 2025, MNRAS[arXiv:2510.25829]

Davies, F. B., Bosman, S. E. I., Gaikwad, P., et al. 2023, arXiv e-prints, arXiv:2312.08464

Davies, F. B., Bosman, S. E. I., Gaikwad, P., et al. 2024, ApJ, 965, 134

Davies, F. B. & Furlanetto, S. R. 2016, MNRAS, 460, 1328

Davies, F. B., Hennawi, J. F., Bañados, E., et al. 2018, ApJ, 864, 142

Dayal, P. & Ferrara, A. 2018, Phys. Rep., 780, 1

D’Odorico, V., Bañados, E., Becker, G. D., et al. 2023, MNRAS, 523, 1399

Fan, X., Strauss, M. A., Becker, R. H., et al. 2006, AJ, 132, 117

Gaikwad, P., Haehnelt, M. G., Davies, F. B., et al. 2023, MNRAS, 525, 4093

Gaikwad, P., Rauch, M., Haehnelt, M. G., et al. 2020, MNRAS, 494, 5091

Gallerani, S., Ferrara, A., Fan, X., & Choudhury, T. R. 2008, MNRAS, 386, 359

Gnedin, N. Y., Becker, G. D., & Fan, X. 2017, ApJ, 841, 26

Gnedin, N. Y. & Madau, P. 2022, arXiv e-prints, arXiv:2208.02260

Greig, B., Mesinger, A., & Bañados, E. 2019, MNRAS, 484, 5094

Greig, B., Mesinger, A., Bañados, E., et al. 2024, MNRAS, 530, 3208

Greig, B., Mesinger, A., Davies, F. B., et al. 2022, MNRAS, 512, 5390

Hoag, A., Bradac, M., Huang, K., et al. 2019, ApJ, 878, 12

Jin, X., Yang, J., Fan, X., et al. 2023, ApJ, 942, 59

Jones, G. C., Bunker, A. J., Saxena, A., et al. 2025, MNRAS, 536, 2355

Kageura, Y., Ouchi, M., Nakane, M., et al. 2025, ApJS, 278, 33

Kashino, D., Lilly, S. J., Shibuya, T., Ouchi, M., & Kashikawa, N. 2020, ApJ, 888, 6

Keating, L. C., Kulkarni, G., Haehnelt, M. G., Chardin, J., & Aubert, D. 2020, MNRAS, 497, 906

Kulkarni, G., Keating, L. C., Haehnelt, M. G., et al. 2019, MNRAS, 485, L24

Maity, B. & Choudhury, T. R. 2022a, MNRAS, 511, 2239

Maity, B., Davies, F., & Gaikwad, P. 2025, arXiv e-prints, arXiv:2505.09369

Mason, C. A., Treu, T., Dijkstra, M., et al. 2018, ApJ, 856, 2

McQuinn, M. 2016, ARA&A, 54, 313

Morales, A. M., Mason, C. A., Bruton, S., et al. 2021, ApJ, 919, 120

Nasir, F. & D’Aloisio, A. 2020, MNRAS, 494, 3080

Planck Collaboration, Aghanim, N., Akrami, Y., et al. 2020, A&A, 641, A6

Qin, Y., Mesinger, A., Prelogović, D., et al. 2025, PASA, 42, e049

Sobacchi, E. & Mesinger, A. 2015, MNRAS, 453, 1843

Spina, B., Bosman, S. E. I., Davies, F. B., Gaikwad, P., & Zhu, Y. 2024, A&A, 688, L26

Spina, B., Bosman, S. E. I., Maity, B., & Davies, F. B. 2025, arXiv e-prints, arXiv:2507.12170

Trac, H., Chen, N., Holst, I., Alvarez, M. A., & Cen, R. 2022, ApJ, 927, 186

Umeda, H., Ouchi, M., Kageura, Y., et al. 2025a, arXiv e-prints, arXiv:2504.04683

Umeda, H., Ouchi, M., Kikuta, S., et al. 2025b, ApJS, 277, 37

Umeda, H., Ouchi, M., Nakajima, K., et al. 2024, ApJ, 971, 124

Vernet, J., Dekker, H., D'Odorico, S., et al. 2011, A&A, 536, A105

Wang, F., Davies, F. B., Yang, J., et al. 2020, ApJ, 896, 23

Zel'dovich, Y. B. 1970, A&A, 5, 84

Zhu, Y., Becker, G. D., Bosman, S. E. I., et al. 2024, MNRAS, 533, L49

Zhu, Y., Becker, G. D., Bosman, S. E. I., et al. 2021, ApJ, 923, 223

Zhu, Y., Becker, G. D., Christenson, H. M., et al. 2023, ApJ, 955, 115

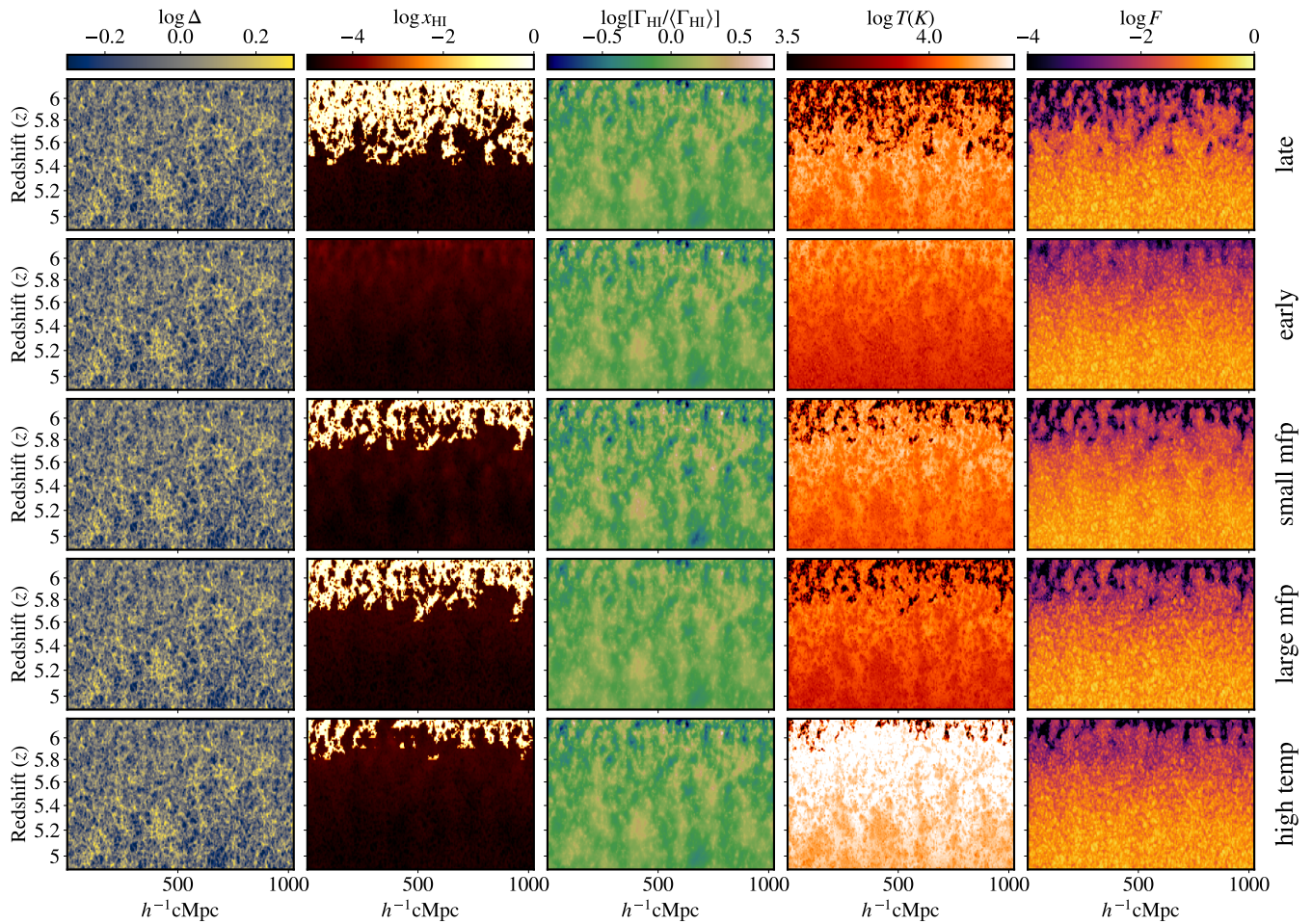


Fig. A.1. Lightcone snapshots for the rest of the five cases complementing Figure 2 (i.e., "late", "early", "small mfp", "large mfp" and "high temp", respectively from top to bottom). The columns correspond to density (Δ), neutral fractions (x_{HI}), UVB fluctuations ($\Gamma_{\text{HI}}/\langle\Gamma_{\text{HI}}\rangle$), temperature (T), and flux (F). The colorbars have been shown in logarithmic scales.

Appendix A: Snapshots for the rest of the scenarios

In Figure A.1, we show the lightcone snapshots of the different physical quantities for the rest of the scenarios, complementing Figure 2. It is apparent that the "late" reionization end shows an abundance of neutral patches at a redshift as low as $z \sim 5.4$, while the "early" scenario ends before $z \sim 6.1$. Similarly, "small mfp" and "large mfp" provide slightly enhanced and reduced UVB fluctuations, respectively. The enhancement in temperature is also visually well distinguishable for the "high temp" model from the others.